Journal of Microscopy, Vol. 202, Pt 3, June 2001, pp. 518–532.
Received 18 September 2000; accepted 6 December 2000

Micromechanical and structural properties of a pennate diatom investigated by atomic force microscopy

N. ALMQVIST*†§, Y. DELAMO‡**, B. L. SMITH†, N. H. THOMSON†¶, Å. BARTHOLDSON*, R. LAL§, M. BRZEZINSKI‡ & P. K. HANSMA†

**Department of Physics, Luleå University of Technology, SE-971 87 Luleå, Sweden*
†Department of Physics, ‡Marine Science Institute, §Neuroscience Research Institute, University of California, Santa Barbara, California 93106, U.S.A.
¶Department of Physics and Astronomy, University of Leeds, Leeds LS2 9JT, U.K.
***Laboratoire d'Océanographie Biologique (LOB), UMR CNRS 5805 – Université Bordeaux 1, Station Marine d'Arcachon, 2 rue du Professeur Jolyet, F-33120 Arcachon, France*

Key words. AFM, Atomic force microscopy, biomineralization, diatom, elasticity, hardness, nanoindentation, *Navicula pelliculosa*.

Summary

The mechanisms behind natural nanofabrication of highly structured silicas are increasingly being investigated. We have explored the use of a standard Nanoscope III Multimode atomic force microscope (AFM) to study the silica shell of diatoms. The delicate structures of the shell surface of the diatom *Navicula pelliculosa* (Bréb.) Hilse were imaged and the shell's micromechanical properties were measured semi-quantitatively with a resolution down to approximately 10 nm. The technique to measure elasticity and hardness with the AFM was demonstrated to be useable even on these hard glass-like surfaces. Different experimental configurations and evaluation methods were tested. They gave a consistent result of the shell micromechanical properties. The first results showed that the diatom shell's overall hardness and elasticity was similar to that of known silicas. However, regions with different mechanical properties were distinguished. The elastic modulus varied from 7 to 20 GPa, from 20 to 100 GPa and from 30 to hundreds of GPa depending on the location. In general, the hardness measurements showed similar spatial differences. The hardness values ranged from 1 to 12 GPa but one specific part of the shell was even harder. Hence, certain localized regions of the shell were significantly harder or more elastic. These regions coincide with known characteristic features and mechanisms appearing at the different stages of the shell's growth. These results show that this method serves as a complementary tool in the study of silica biomineralization, and can detect eventual crystalline phases.

Correspondence: N. Almqvist. Tel.: + 46 92072291; fax: + 46 920 91074; e-mail: Nils.Almqvist@mt.luth.se

Introduction

Biomimetics is a new science of synthesizing new and better composite materials by mimicking natural mechanisms of biomineralization. One example is the abalone nacre, which consists of single crystal tablets of aragonite, cemented together by thin layers of organic material. It requires 3000 times more work to fracture abalone nacre than geological aragonite. Therefore, models have been proposed for the nacre growth (Schaffer *et al.*, 1997) and the elastic properties of the nacre organic material have been measured (Smith *et al.*, 1999). Moreover, attempts have been made to construct synthetic materials with structures similar to that of the nacre (Almqvist *et al.*, 1999).

A related group of materials is synthetically derived silica-based materials. Natural silicas can be found in unicellular algae and appear as highly sculptured silicates. Research has started to reveal the mechanisms for their synthesis (Morse, 1999). Diatoms (Bacillariophyceae) are suitable for studies of biomineralization and they can inspire new approaches to silica production (Vrieling *et al.*, 1999). There is a growing demand for mesoporous silicas for use as, for example, filter agents, ion-exchange materials and abrasives. Hence, structural and micromechanical information on diatoms is important, especially the correlation of the nanofabricated structures to physical properties and theories of growth mechanisms. Previously, it has been demonstrated that contact-mode atomic force microscopy (AFM) can be used for structural studies of diatoms in air (Linder *et al.*, 1992). The advantages of AFM compared to traditional scanning electron microscopy (SEM) imaging are the high resolution, three-dimensional imaging and the ability to study the delicate valve margin with a minimum

of sample preparation. Atomic force microscopy makes it possible to measure structural and physical properties with the desired spatial resolution. The accuracy of quantitative results from AFM nanoindentation or elastic measurements has been the subject of discussion, but even relative micromechanical data are of great importance.

Diatoms are unicellular, eukaryotic protists (Round *et al.*, 1990). They are pigmented, photosynthetic and live in both marine and freshwater. The characteristic of diatoms is their ability to produce a siliceous cell wall or shell, which presents highly detailed species-specific elaborately patterned microstructures. Besides silica, the diatom wall is surrounded by an organic thin coating, and only a small amount of metals. The cell wall is formed of two overlapping halves (valves), which are linked together by thin circular silica girdle elements. The wall components are collectively termed the frustule. The lower part of the frustule, termed the hypovalve, is smaller than the upper and outer part of the frustule, the epivalve. During cell division, the epitheca and hypotheca move apart as new valves are synthesized. Following daughter cell separation new girdle bands are deposited to complete the frustule of the two new daughter cells. The frustule may have a complex structure and usually has fine openings in the cell wall (pores) or openings covered with a thin membrane (poroids). At present, between 12 000 (Werner, 1977) and 60 000 (Gordon & Drum, 1994) diatom species have been identified around the world, each of them having its own specific intricate morphology. There are two major groups of diatoms, divided on the basis of their symmetry: centric diatoms have a radial symmetry, and pennate diatoms have a bilateral symmetry. Diatoms secrete large amounts of extracellular polymeric substances (essentially polysaccharides, see Hoagland *et al.*, 1993). Most pennate diatoms possess a longitudinal slit in the valve called a raphe, which is related to their ability to adhere to a substratum and glide across. The structure (Schoeman *et al.*, 1976) and shell formation (Chiappino & Volcani, 1977) of the freshwater pennate diatom *Navicula pelliculosa* (Bréb.) Hilse, used in the present work, has been extensively studied. It has been proposed that organic macromolecules participate in the precipitation of silica and influence the morphogenesis of the cell wall (Robinson & Sullivan, 1987; Pickett-Heaps, 1990). The primary structure for some of the *N. pelliculosa* cell-wall proteins has also been determined (Van de Poll *et al.*, 1999). However, little is known about the detailed pathways of cell wall formation. Increased knowledge of the frustule mechanical properties and morphogenesis may help us to understand the organic and inorganic processes involved in silica biomineralization.

The aim of the present work was to explore the possibilities of the atomic force microscope as a complementary technique in the study of diatoms and biomineralization, and to measure micromechanical properties of the small but extensively studied model diatom *N. pelliculosa*.

Experimental materials and methods

The diatom species *N. pelliculosa* was obtained from Scripps Research Institute, San Diego, through the courtesy of Dr M. Hildebrand. The culture was maintained at 17 °C under a continuous photon fluence rate of approximately 100 $\mu E\ m^{-2}\ s^{-1}$, in liquid freshwater tryptone (FWT) medium (Reimann *et al.*, 1966). For the purpose of the experiments, the diatoms were plated on a FWT medium solidified with 1.5% agar and further grown under the above described conditions. After about 10 days, some cells were transferred into different substrate-covered steel-plates by applying the plates against the visible colonies. The plates were then either directly imaged on the atomic force microscope or transferred into liquid FWT medium for further diatom growth. The diatoms from the FWT medium were prepared by several different methods for AFM measurements. For plain imaging, they were allowed to grow on a substrate surface, rinsed, eventually dried and transferred to the microscope for imaging in liquid or under ambient conditions. The micromechanical properties were measured on dried samples. These samples were rinsed in ethanol, to prevent growth of microorganisms, and dried. In general, decay and bacteria removes much of the organic material.

Macroscopic Vickers hardness on reference surfaces was measured with a commercial microhardness tester (Matsuzawa MXT-CX, Ota-ku, Tokyo). The microscopes used were three commercial Nanoscope III Multimode (Digital Instruments, Santa Barbara, U.S.A.) microscopes. Several different types of cantilever were used for the studies. Standard silicon tapping-mode tips (Digital Instruments) and silicon or silicon nitride contact-mode tips (ThermoMicroscopes; Sunnyvale, CA; Digital Instruments) were used for plain imaging and simple mechanical measurements, respectively. We assumed the silicon tip to have a Young's modulus of 150 GPa and a Poisson ratio of 0.17. To fine-tune and stiffen the standard silicon diving board cantilevers, cold steel weld resin (J-B Weld, Sulphur Springs, Texas, U.S.A.) was attached to the back side, towards the base, of the blade-like tipped silicon cantilevers. We used the commercially available diamond tipped stainless steel cantilevers from Digital Instruments for nanoindentation. The tip was assumed to have an outermost radius of 25 nm, as specified by the manufacturer. This assumption was verified by scanning the tip over sharp surface steps and inspecting the images. We concluded that it was smaller than 40 nm. To calibrate the stiffer cantilevers, we constructed a calibration spring. One end of a tungsten wire was glued, at approximately 45°, onto a steel plate. On the other end we glued a small, approximately 1 mm^2, mica 'landing

plate'. The spring constant of the tungsten spring was determined by pressing it against a microbalance with a micropositioner and monitoring the force as a function of the position. The reference spring constant, K_{ref}, was determined as 143 ± 2 N m^{-1} (mean $\pm$ SD). To determine the spring constant for the actual cantilever, we recorded force curves on a 'hard' surface and on the reference spring. The spring constant, K, is extracted from the system of two linear springs in series simply as:

$$K = K_{ref}\left(\frac{\lambda_{hard} - \lambda_{tot}}{\lambda_{tot}}\right), \quad (1)$$

where λ_{hard} and λ_{tot} are the slopes of the force curve on the hard surface and the reference spring, respectively. Our stainless steel cantilever was shown to have $K = 125$ N m^{-1}.

Micromechanical measurements

General considerations and software

In a typical elasticity or indentation experiment, the sample is raised into contact with the probe tip, then further raised to press the tip into the surface. Finally, the sample is lowered to withdraw the tip from the surface. The z-piezoelectric scanner controls the vertical motion simultaneously as load-displacement data, the so-called force curve, are recorded. One concern about the accuracy of the measurement is about the z-piezo-scanner. Piezo-scanners are known to possess nonlinearity, creep and hysteresis, therefore introducing an uncertainty in the tip position. There are also concerns about the deflection detection system, accurate measurements of the cantilever spring constant, linearity of the segmented photodiode output and the non-normal loading of the tip against the surface (further discussed below). The use of very sharp tips for indentation may also be a problem. They can introduce additional loss of energy due to cracking and cutting of the sample. To achieve high precision quantitative data one has, at least, to calibrate the system on a sample with known micromechanical properties.

Calibration of the AFM deflection detection system is crucial for precise measurement of the forces used. The cantilever deflection, i.e. the AFM photodetector signal, is calibrated by taking AFM force curves on a hard surface. The force, F, exerted by the cantilever is simply the product of the cantilever spring constant and the cantilever deflection. In this work we calibrated the cantilever deflection at low loads on Si(111) but very hard material such as sapphire is sometimes preferable. Our experience is that calibration from single force curves can deviate considerably and give a systematic error in the measured forces of as much as 5–10%. Therefore, we recalibrated the deflection off-line by averaging to force curves at different locations on the hard reference surface, typically about 1000 force curves.

The Nanoscope software version 4.23 was used for general image analysis. The AFM force curves were imported and analysed with tools developed within the IGOR Pro (Wavemetrics, Lake Oswego, OR) data analysis software. The set of tools are originally based on the IGOR Pro SPM tools developed separately by J. Guyer in 1999 (http://www.his.com/~jguyer/IGOR/) and D. Laney (Laney *et al.*, 1997), but the major part has been developed and integrated to a procedure in our laboratory. Using the procedure we are able to evaluate whole force–volume images, i.e. a raster scanned array of force curves, and present elastic, indentation or surface hardness maps. The procedure automatically finds the contact point, where the tip makes contact with the surface, in each force curve by analysis of the second derivative in combination with several error-checking functions.

The elastic modulus was generally evaluated on force curves with low maximum load, without any visible plastic deformations of the surface. We also verified that both elasticity and surface hardness could be extracted from force curves recorded at higher maximum loads. Then, the tip-sliding and other effects in AFM measurements, such as piezo hysteresis and creep, complicated the analysis. Thus, we recorded the reference force curves at low loads with only the elastic response of the surface. When the surface response is purely elastic, the load and unload curves should follow each other. This feature was used to correct the unload curve on the diatom sample by multiplying with the load-specific correction factors. The correction factors were extracted with identical instrumental set-up and at the same maximum load as was used on the measured sample.

Hardness, nanoindentation

Nanoindentation with AFM is similar to conventional hardness testing but on a very small scale and with a high spatial resolution. The hardness of a surface is proportional to the yield stress of the material. In the simplest form, the hardness is measured by making indentation marks in quasi-static mode. Tapping-mode imaging with the same probe is used to measure the geometry of the residual impressions. The depth or area of the indentations is used to calculate the hardness. However, indentation is a complex process and there is no generally accepted definition of hardness. Several different values are frequently used. More or less conventional atomic force microscopes have been used to measure micromechanical properties of many materials (Burnham & Colton, 1989; Bhushan & Koinkar, 1994; Nakajima *et al.*, 1996; Randall *et al.*, 1996; Vanlandingham *et al.*, 1997a, b; Gracias & Somorjai, 1998) in quasi-static mode. Add-on improvements to the standard microscope (Bhushan *et al.*, 1996) have been used

to probe local nanohardness and elasticity on many solid materials, for example polymers (Nie *et al.*, 1995), bones, alloys (Göken & Kempf, 1998), polycrystalline materials (Bhushan & Koinkar, 1996) and metals (Kempf *et al.*, 1998).

One of the problems when using the standard microscope for nanoindentation is the cantilever-mounting angle, approximately 12° to the surface. This causes a small lateral slide of the cantilever, and an additional bending, as it approaches the surface. In this work, we slowly scan the tip laterally in a raster pattern simultaneous to the vertical loading, in what is known as force–volume imaging. By choosing the appropriate scan parameters, typically lateral scan of about 600 nm s^{-1}, the tip-sliding was approximately eliminated during tip–surface approach in alternate scan-lines, i.e. every second row of indents. The hardness is computed as the mean pressure at maximum load:

$$H = \frac{F}{A} = \alpha \frac{F}{{h_m}^2} \tag{2}$$

Here F is the maximum applied force, h_m is the indentation depth and α is a constant. For the ideal Berkovich or Vickers indenter $\alpha = 1/24.5$. The geometry of the diamond tip is, however, slightly more complicated because it is specified to have a tip opening angle of 60°.

For several commonly used indenter geometries, the strain caused by the indent is only a function of the indenter's geometry. However, this is not the case for a spherical indenter where the contact radius is also an important parameter. To quantitatively analyse the hardness, we calibrated the hardness values measured with the three-sided Berkovich-type indenter against the macroscopic Vickers hardness (*VH*) from the microindenter. The *VH* hardness in the microindenter is quoted as the ratio between the applied force and the facial contact area of the four-sided Vickers indenter. Hence, the Vickers hardness is:

$$VH = \frac{F}{d^2/2\sin\left(\frac{\psi}{2}\right)} \tag{3}$$

Here d is the diagonal of the residual indent and ψ is the angle between two faces of the indenter (i.e. 136°). For Berkovich indenters it is common to use the projected area. Hence, the relation between the Berkovich, VH_P and Vickers hardness for this indenter is:

$$VH_P = \frac{1}{\sin\left(\frac{\psi}{2}\right)} VH \tag{4}$$

Although the indenter geometries are slightly different, we used VH_P to calibrate the hardness measured with the microscope, V_{AFM}, by introducing a calibration factor $c = VH_P/V_{AFM}$. To further reduce the effect of different geometries, even spherical, we indented both the calibration surface (i.e. mica or silicon) and the sample at same applied load, and hence similar contact geometry, and calculated c for each load. The sample nanohardness is $c \cdot V_{AFM}$.

Evaluation of the force–displacement curves, obtained during indenting, provides further information to evaluate additional mechanical properties. The total work, i.e. the sum of the plastic and elastic work, from the AFM tip on the sample is the area under the loading curve in the force–distance diagram. Together with Eq. (2) this gives for the total work:

$$W = \int_{h=0}^{h_m} F\mathrm{d}h = \frac{H{h_m}^3}{3\alpha} \tag{5}$$

If we assume that the hardness depends only on the plastic work, W_P we can use Eqs (2) and (5) to calculate the hardness as:

$$H = \frac{\alpha F^3}{9{W_P}^2} \tag{6}$$

This expression was used on the whole array of indentation force curves to produce a hardness image of the sample. Again, all values were adjusted to reproduce the macroscopic hardness values on the surrounding substrate (in this case mica). Some work has been carried out with considerations of eventual shoulders, pile-up and sink-in, around the indents (Drechsler *et al.*, 1998). The atomic force microscope is a very useful tool for measuring all the involved volumes to improve the hardness calculations. This is, however, outside the scope of this paper.

Elasticity

We used Sneddon mechanics, which describe the indentation of an elastic half space due to different indenter geometries (Sneddon, 1965; Vanlandingham *et al.*, 1997a) to relate the indentation depth δ of the sample to the applied force F:

$$F = \frac{\varepsilon E}{(1-\upsilon^2)}\delta^n, \tag{7}$$

where ε depends on the punch geometry, E is the elastic modulus, the exponent n is related to the indentation geometry and υ is the Poisson ratio. We assumed $\upsilon = 0.17$ for the diatoms. At small indentation depths, as in this work, we approximated the AFM tip as a spherical punch with tip radius R, which is described by $n = 3/2$. Then Eq. (7) becomes:

$$F = \frac{4E}{3(1-\upsilon^2)}\sqrt{R}\delta^{3/2} \tag{8}$$

The elastic modulus was calculated from the AFM force curves with two different methods:

(a) In the indentation method the penetrations were calculated for each point of the samples force–distance curve as the difference between this curve and the hard

reference curve (see for example Radmacher *et al.*, 1994; Radmacher *et al.*, 1995; Ikai, 1996; Weyn *et al.*, 1998). Linear regression with the model in Eq. (8) was used to extract E.

(b) In the deflection method (Radmacher *et al.*, 1996) we directly use the fact that Eq. (8) can be reformatted to give:

$$z - z_0 = d - d_0 + \left[\frac{3k(1-\upsilon^2)}{4E}\right]^{\frac{2}{3}} R^{-\frac{1}{3}}(d-d_0)^{\frac{2}{3}} \qquad (9)$$

Here z_0 and d_0 are the contact point and the free deflection value, respectively. Numerical nonlinear regression was used to extract the two parameters E and z_0 from the model.

If the elastic modulus of the tip is much larger than that of the sample, the elastic modulus of the latter, E_S, can be approximated by the measured modulus E. Otherwise, it is corrected according to the frequently used relation:

$$\frac{1}{E} = \frac{1-\nu_{tip}}{E_{tip}} + \frac{1-\nu_s}{E_s}, \qquad (10)$$

where E_{tip} is the elastic modulus of the tip, ν_{tip} and ν_s are the Poisson ratio of the tip and sample, respectively.

Results

Imaging

The sample preparation for imaging in fluid was more troublesome than the preparation for imaging in air. Most of the results shown in this paper are therefore on diatoms that have been grown on a mica surface in the FWT medium and are imaged under ambient conditions. Plain 'dried' diatoms stay alive on the surface for a few hours. Figure 1(a) shows, with a schematic drawing, the different parts of a diatom frustule. The basic structure of the frustules of *N. pelliculosa* has been described by others (Busby & Lewin, 1967; Schoeman *et al.*, 1976; Chiappino & Volcani, 1977). The remaining images in Fig. 1 show the diatom structure as observed with tapping-mode AFM under ambient conditions. Figures 1(b)–(d) show surface plots of the whole valve of diatoms prepared with two different methods. The sample in Fig. 1(b) was prepared by mechanical transfer of diatoms to a silanized (3-amino-propyltriethoxysilane) mica surface and imaged as soon as possible in air. In Figs 1(c) and (d), the diatoms were directly grown and imaged on the same surface, after ethanol rinsing. The complex structure with pores or poroids is easily resolved with AFM. The diatom valve is elliptical, or linear-elliptical, with rounded ends. Each valve is split along its longitudinal, called apical, axis by the raphe fissure (RF), with a characteristic bent shape at its ends. The central ribs (CR) enclose the raphe. The rectangular sieve plates or puncta (pores and poroids) together form bands of striae between the central ribs (CR) and the valve edge. Moreover, as seen in the figure, the puncta coalesce into elongated slits towards the edge of the valve. It is well known that such structures on sharp edges can be difficult to interpret with AFM due to probe tip effects. However, we scanned diatoms standing on their edge (not shown) and verified the existence of the elongated slits.

The high-resolution AFM imaging is limited to image sizes of about 100 nm, partly due to remaining organic coating. The microstructure is fairly smooth with shallow hillocks, 10–20 nm in diameter and 1–2 nm high, uniformly distributed over the frustule. On most frustules they are slightly larger towards the centre of the shell and show up with higher contrast in AFM phase imaging (not shown). These structures may be the remains of the knolls visible in the early growth stages of the shell (Chiappino & Volcani, 1977).

Traditionally, diatom morphology and taxonomy are studied by SEM or transmission electron microscopy. Such techniques may require the oxidation of the organic material of diatom cells or the mounting and coating of the cells before observation. If not cleaned, the outer organic coating will obscure most details. Lightly silicified diatoms may often collapse with those treatments. Also our preparation methods sometimes made the diatoms collapse or separate into their constituent parts. For example, the image in Figs 1(b) and (c) shows only one of the valves. The image most likely shows the epitheca in an inside view with a remaining girdle band. The AFM images clearly resolve the girdle bands, also shown in Fig. 1. Figure 2(a) shows the separated epitheca and hypotheca of one cell. The raphe ends of the two cells are bent in reversed directions in this valve view. The figure also shows nanoindentation, on the same frustule, which is discussed in the next section.

Imaging in liquid requires tight anchoring of the diatoms to the substrate. In general, pennate diatoms adhere to surfaces by polysaccharide material, held together by mucilage pads. *N. pelliculosa* do not form chains, but only attach loosely to our substrates, even when we grow them in tissue culture Petri dishes. The diatoms have to be immobilized on the substrate. Still, the resolution in AFM

Fig. 1. (a) Schematic drawing of a diatom frustule; CR = central rib; CN = central nodule; TR = transapical rib; RF = raphe fissure; CRF = curved end side of the raphe fissure. (b–e) AFM tapping-mode surface plots of diatom shells. The plots have a mixture of virtual illumination and colour-coding. (b) The sample was prepared by mechanically transferring diatoms to a silanized surface and then imaging as soon as possible under ambient conditions. The total vertical z-scale is 2 μm. (c–d) Different diatoms from the same sample prepared by growing diatoms on a mica surface and rinsing in ethanol and drying. The total vertical scales are 1.2 μm and 4 μm in (c) and (d), respectively. (e) Fine structure and one of the puncta of the diatom in (d).

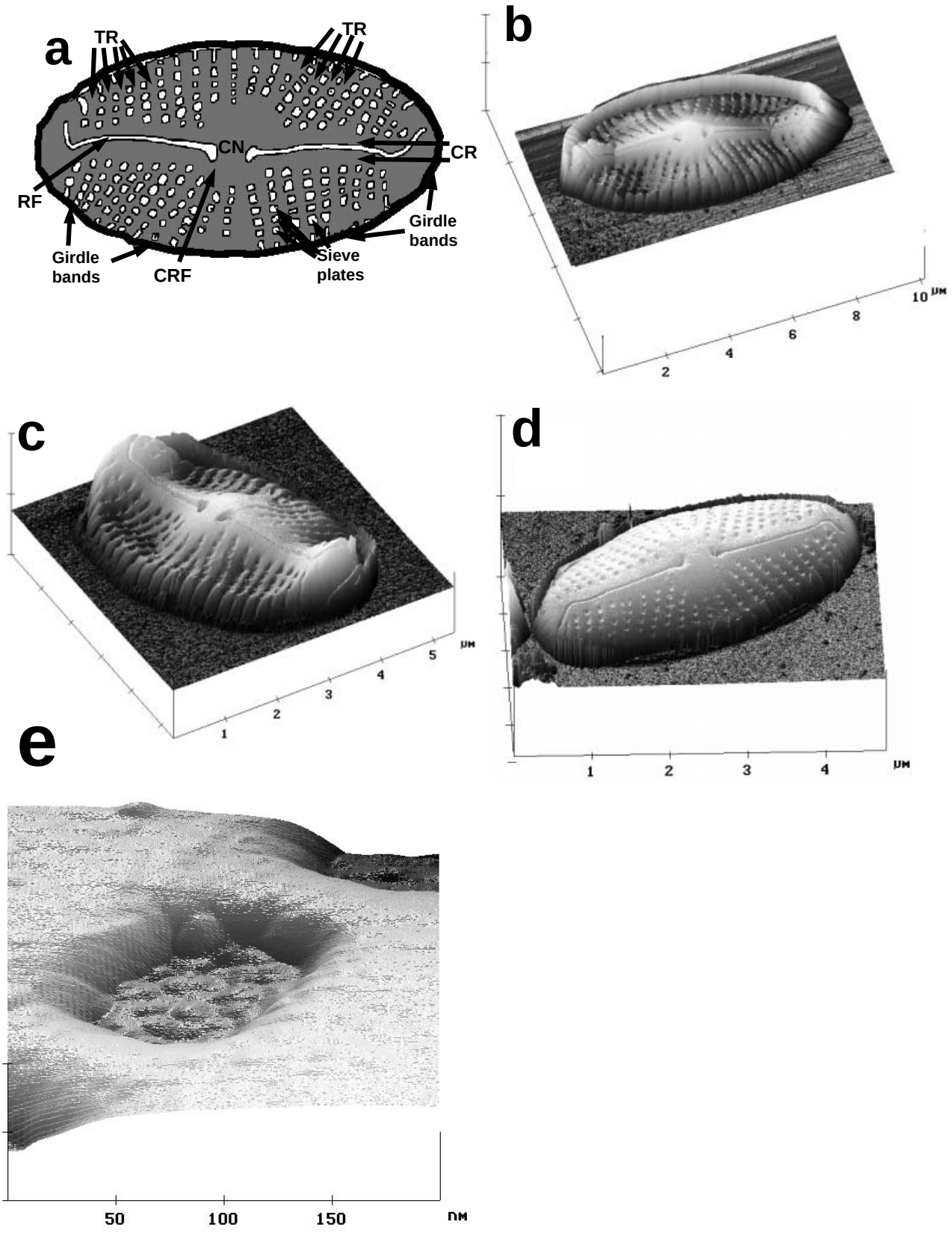
a
TR
TR
CN
CR
RF
Girdle bands
Girdle bands
CRF
Sieve plates
b
10 µm
8
6
4
2
c
µm
5
4
3
2
1
d
1
2
3
4
µm
e
50
100
150
nm

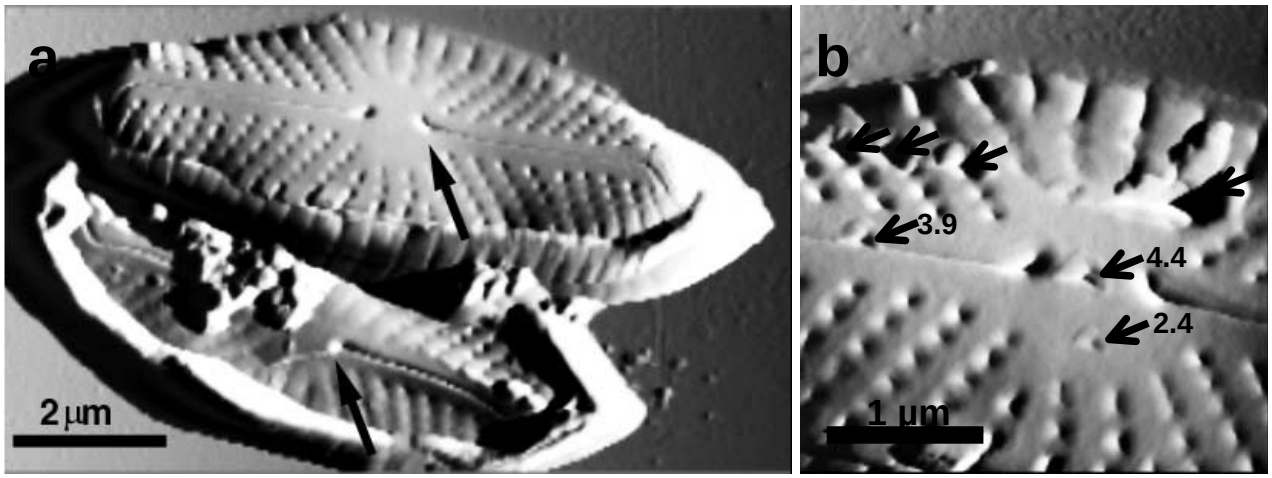

Fig. 2. AFM tapping-mode amplitude image of diatom valves. (a) The separated valves. (b) Nanoindentation of the same valve, at different forces 25–62 μN, with the silicon tip. The approximate hardness values at three locations (arrows) are given in GPa.

liquid imaging was reduced due to disturbances from the sticky mucilaginous organic coating, especially in the very sensitive tapping-mode in liquid. Some of the geometry measurements and profiles of diatoms in buffer were done on the mechanically transferred diatoms with subsequent immersion into buffer.

AFM cross-sectional profiles, each from a different diatom, are shown in Fig. 3(a). The profiles reveal the characteristic shape with girdle bands at the edges of the valves and sometimes the transapical rib (TR) region collapsing from drying. Volume and geometric measurements on 10 moderately sized non-collapsed isolated diatoms are shown in the graph in Fig. 3(b). The diatom volume, V, has approximately a linear relationship to $l{\cdot}b{\cdot}h$, where l, b and h are the semi-axis of the diatom (i.e. half its length, width and height). Linear regression reveals that $V = 3.3{\cdot}l{\cdot}b{\cdot}h$, surely a fairly ellipsoidal shape.

Phase-angle changes, due to tip–sample interactions, in tapping-mode are sometimes known to produce higher resolution images than the standard height or amplitude images. Figure 4 shows large-scale phase images of three different diatom cells. The images indicate a different phase response at the central nodule region and at the frustule ends. Parts of the central ribs also show an increased phase response.

Diatom micromechanical properties

The AFM tip can be used to modify structures in a number of ways and even make nanostructured imprints. Figure 5 shows several holes made in *N. pelliculosa* with a standard tapping-mode silicon tip. The first image illustrates 'hammering' of a diatom. The tip was lowered against the surface while oscillating, 'hammering' holes in the shell. The second image shows the large demolition caused by pressing the non-oscillating tip with a high force against the frustule. Note that the frustule does not collapse when the tip is pressed against the (central nodule) CN with a high force; instead the material is deformed and a large hole is created. The frustule is brittle and it was easy to completely destroy the shell with simultaneous lateral scanning. Still, the structure is stiff and rigid. Therefore, stiff cantilevers were needed for controlled manipulation and for micromechanical measurements. Figure 6 show elasticity images of the diatom's central region calculated from force–volume data collected with a maximum tip-to-surface force of 1.4 μN, the so-called relative trigger level. The standard tapping-mode cantilever, with a measured spring constant of about 24.4 N m^{-1} and a very sharp silicon tip, was used. The maximum penetration of the AFM tip into the sample surface was typically 1.5–4 nm at the CN region, 2.5–5 nm along the CR and 4–8 nm on the TR. No plastic impressions were observed with subsequent tapping-mode imaging. However, a part of the brittle diatom was broken (dark area in the elasticity images) even with this gentle force–volume imaging. Figure 6 shows relative elasticity calculated with a modified version of the force integration to equal limits (FIEL) map (A-Hassan *et al.*, 1998). The force curves are integrated to the same deflection value. Each integrated area is related to the elasticity of the sample at the specific position. Brighter pixels mean higher elastic modulus. However, the grey scale is arbitrary and the values are scaled according to indentation with spherical geometry. The other images show absolute values of the elastic modulus calculated with the described methods. The calculations were based on a spherical indenter with an outermost radius of 10 nm. As expected, the indentation and deflection methods show a similar overall elastic pattern, but there is a difference in absolute values. In average, the deflection method produces 30% higher values

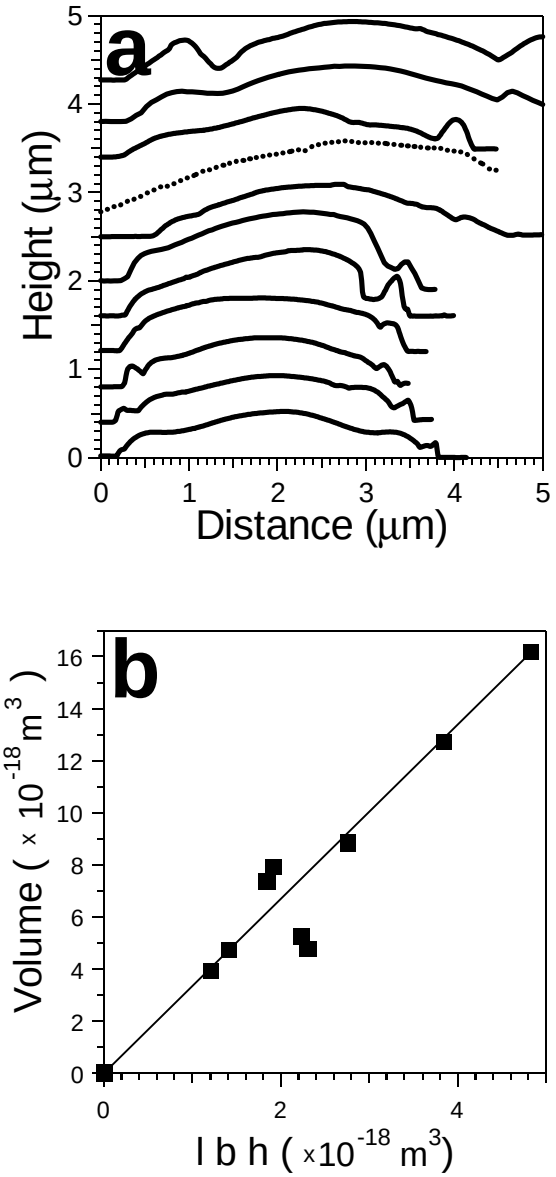

Fig. 3. Geometry of *N. pelliculosa*. (a) AFM cross-section profiles through the central nodule, along the width of several diatoms. The dashed profile is an example of results obtained in liquid. (b) Volume of *N. pelliculosa* as function of $l \cdot b \cdot h$, where l, b and h are the diatom semi-axes.

than the indentation method, but the discrepancy occurs mainly on the hard CN region. Still, the result is fairly clear. The outer TR regions have lower elasticity, values 7–15 GPa and 8–20 GPa for the indentation and deflection methods, respectively. These values have been corrected according to Eq. (10). The corresponding values for the CR regions are 15–30 GPa and 40–110 GPa, and on the CN region from 30 to hundreds of GPa. In particular, the region outside the curved ends of the raphe fissure approaches infinitely stiff values (100–300 GPa).

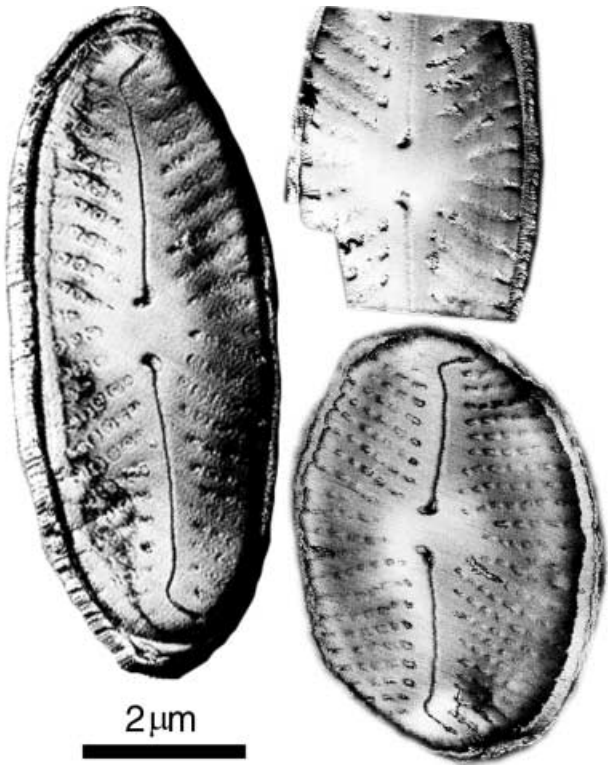

Fig. 4. Large-scale AFM phase images of three different diatom cells. The images show different phase response at different lateral positions on the diatom shell.

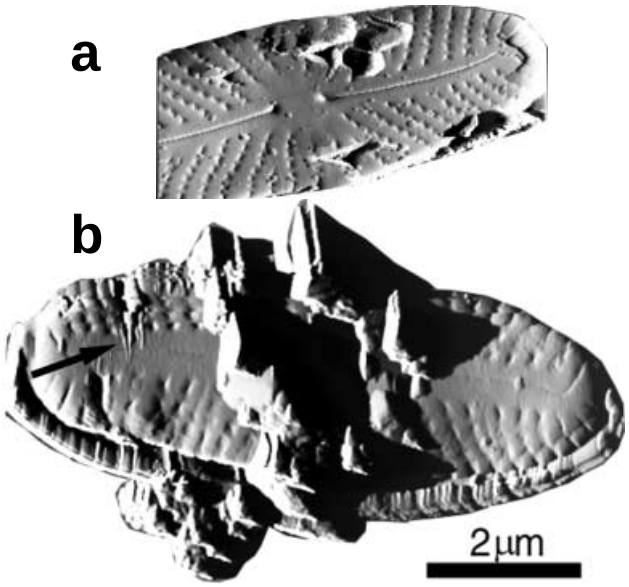

Fig. 5. Example of AFM diatom manipulation with the standard tapping-mode silicon tip. (a) The vibrating AFM tip has been 'hammered' through the frustule at three different spots. (b) Large demolition of the frustule by pressing the tip against the frustule with a very high load. Note also the two scratches that have been made with the tip (arrow).

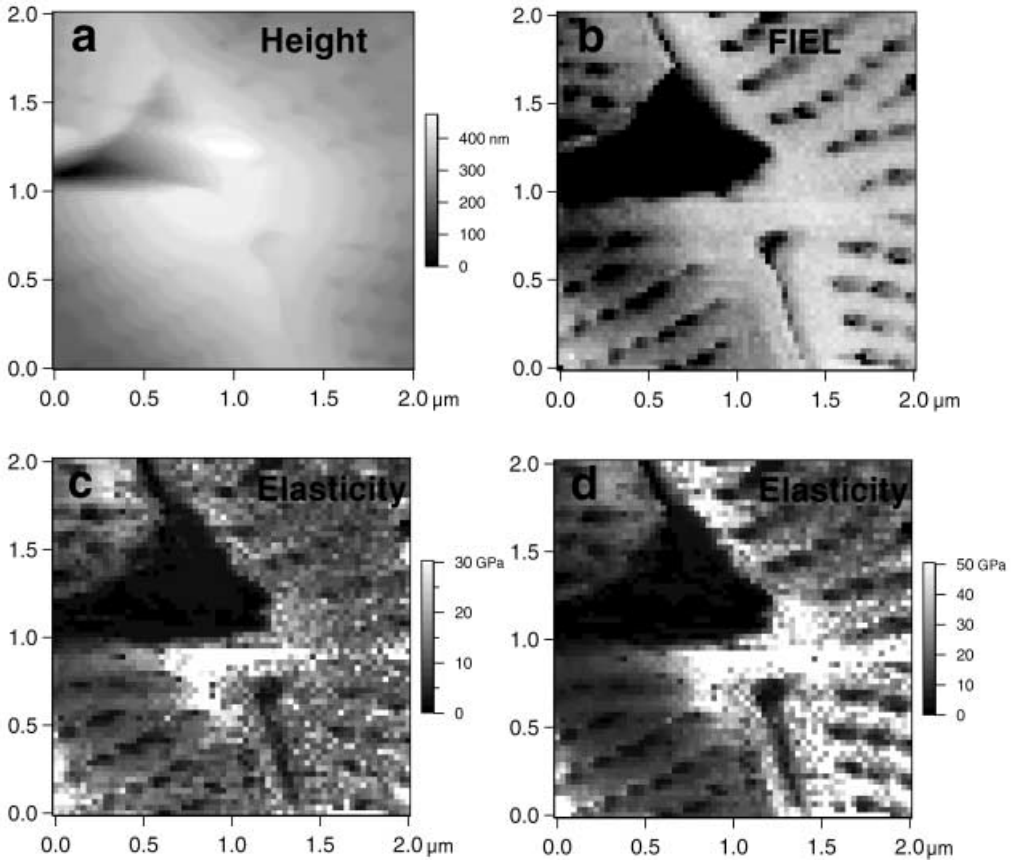

Fig. 6. Elasticity measurements in force–volume mode with a near-standard AFM imaging set-up as described in the text. (a) Height image. (b) FIEL map. (c) Absolute elasticity map calculated with the indentation method. (d) Absolute elasticity map calculated with the deflection method.

The elasticity data from a representative, low-resolution force–volume experiment on another diatom cell, with a stiffer cantilever and a harder tip is shown in Fig. 7. The diamond tip was used at a higher maximum load of 2.3 μN. The figure shows the diatom before the testing and the elasticity, calculated with the deflection method on the unload force curves. The force used is close to, but below, the critical load for plastic deformations. This diatom already had some small cracks, visible in Fig. 7(a). These cracks propagated during the experiment, and show as less stiff regions in the elasticity map. A new crack also developed, seen as a dark spot in Fig. 7(b). Still, the same main features can be distinguished; *N. pelliculosa* has stiff CN and CR regions although the absolute values are lower on this diatom sample. At high forces, the TR regions sometimes collapse, while the CR remains intact.

It is not clear whether we measured the pure shell material elastic property or if the overall geometry contributed. Hence, we also studied the shell surface hardness by making plastic imprints without allowing the shell to crack. In Fig. 2(b) we showed indentations on a diatom, attached on mica, at selected locations (arrows in the figure) with the standard silicon, but spring-constant-tuned, tapping-mode cantilever. The technique is to image the diatoms in the gentle tapping-mode, switch off all scanning and feedback loops. Then apply controlled force curves to create indentations. In this experiment we are sure to probe the local properties, as the applied force is independent of eventual overall frustule deformations, as long as we do not penetrate the AFM tip through the thickness of the frustule. The spring constant used was $294\ \mathrm{N\ m^{-1}}$ and a maximum load of 25–62 μN was applied. The ratio of the maximum applied force to the projected residual area was calculated. The values were corrected with respect to the measured macroscopic Vickers mica hardness (here $c = 0.32$), to yield the hardness values in the figure. Tapping-mode images of indents with the diamond tip are shown in Fig. 8. As shown in the figure, we made indentation on the diatom and substrates at several maximum applied forces. The left column (a–d) shows indentations on reference substrates (mica, silicon), while the second column (e–h) shows indentations on diatoms at the same maximum load. The so-called force–volume mode was used to make the indentations, i.e. the tip was laterally

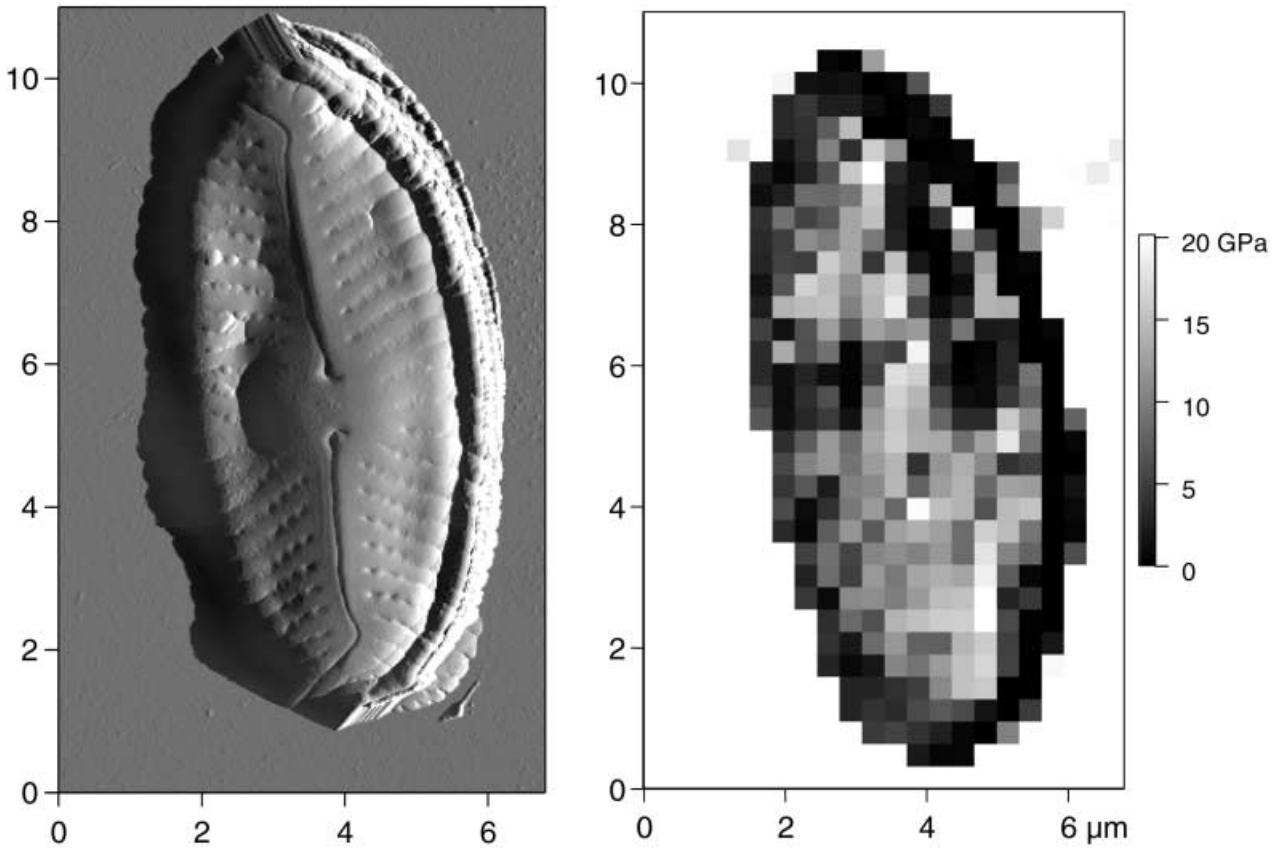

Fig. 7. Elasticity map from force-volume measurements with a diamond tip and a maximum load of 2.3 μN. (a) Tapping-mode amplitude image of the structure before the measurement. (b) The elasticity map (deflection method).

raster-scanned back over the surface simultaneously to the acquisition of the force curves. Hence, we created an equally spaced raster pattern of tip-imprints on the surface. The tip-sliding was approximately eliminated during tip–surface approach in one of the fast-scan directions as described in the *Hardness, nanoindentation* section. For example, of the six indents on mica shown in (a), the middle two indents are with negligible tip-sliding. As is obvious in image (d), the uppermost indent is without, and the lower with, tip-sliding. The hardness values calculated from indents made with significant tip-sliding have a $>$ sign in the figure to indicate that it is a lower limit to the true value. In general, visual inspection of the indents revealed that they are smaller on the CN region than on mica, i.e. the hardness is higher on the CN of *N. pelliculosa*. The hardness also varies with lateral position on the frustule. Clearly, the central node and central rib regions have negligible indentations at the lower loads. The hardness of the surface follows briefly the same pattern as the elasticity. The hardness is high at the CN and CR regions and greatest at a small area near the curved ends of the raphe fissure, where it is higher than measurable in some of our experiments (large indents in image (e)). Note, however, that at the largest indentation depths the calculated hardness is underestimated because the tip passes through the shell (g and h). In general, the hardness on the TR is fairly moderate.

Figure 9 shows the hardness and elastic modulus evaluated from force curves. The maximum load was high enough to produce plastic impressions. The force curves were corrected as described in the section *General considerations and software*. The low-resolution hardness map was calculated according to Eq. (7) and corrected according to the known macroscopic hardness on mica and the measured mica impressions from the same image. The elastic modulus was calculated on the unload curve as previously described. The hardness is high in the CN region, especially in between the curved ends of the RF, and on spots on the CR, with values up to 4.5 GPa and 12 GPa, respectively. High elastic modulus does not completely correlate with high hardness values, but the modulus is also higher on the CN region and on other parts of the CR. The hardness map agrees well with the corrected sample hardness based on Eqs (3) and (4) and shown in Fig. 8. Moreover, the absolute values are fairly consistent with those previously calculated.

Discussion

In this study, AFM was used to investigate the structure and

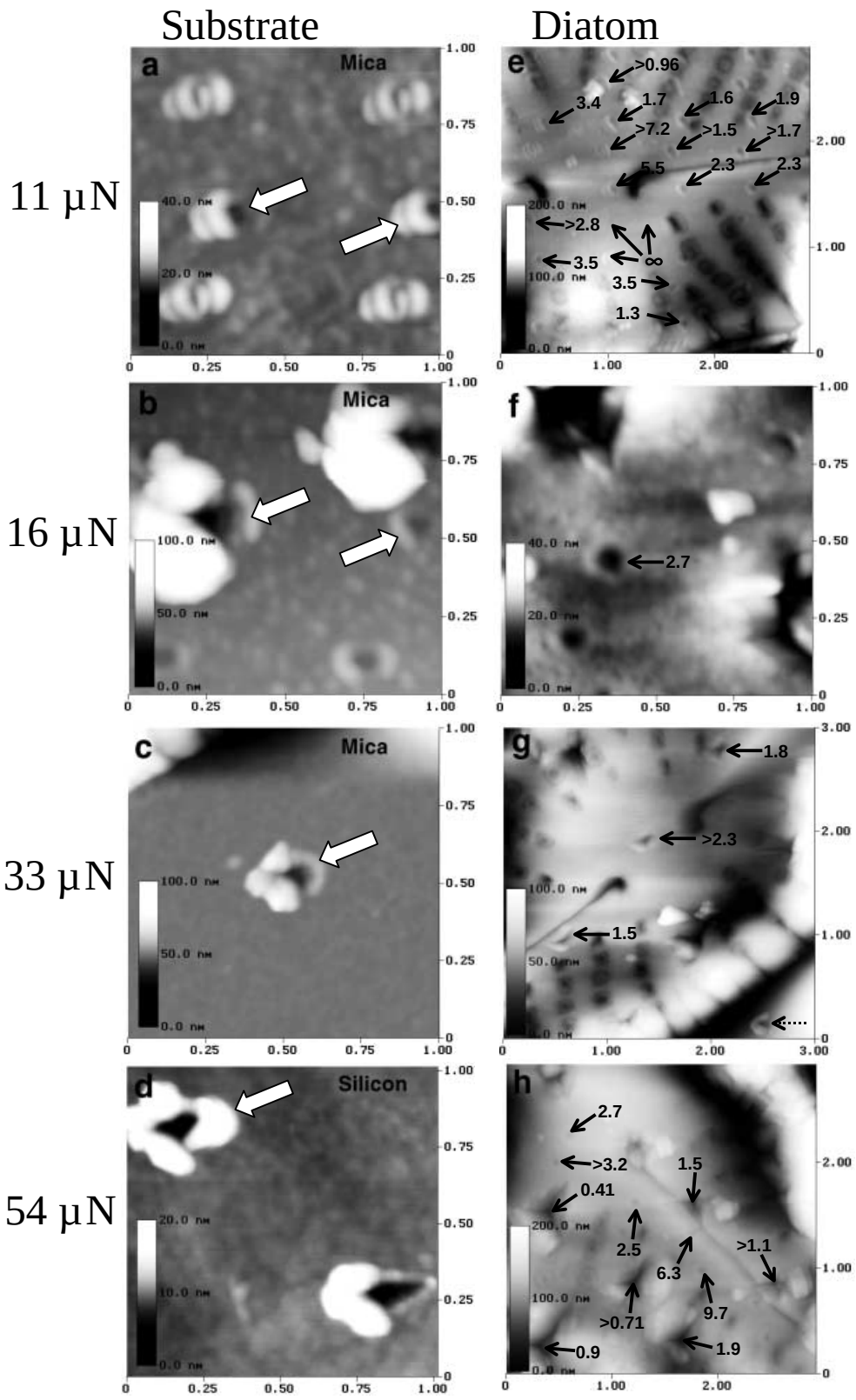
Substrate
Diatom
11 µN
16 µN
33 µN
54 µN
a
Mica
b
Mica
c
Mica
d
Silicon
e
f
g
h
>0.96
3.4
1.7
1.6
1.9
>7.2
>1.5
>1.7
5.5
2.3
2.3
>2.8
3.5
∞
3.5
1.3
2.7
1.8
>2.3
1.5
2.7
>3.2
1.5
0.41
2.5
6.3
>1.1
>0.71
9.7
0.9
1.9

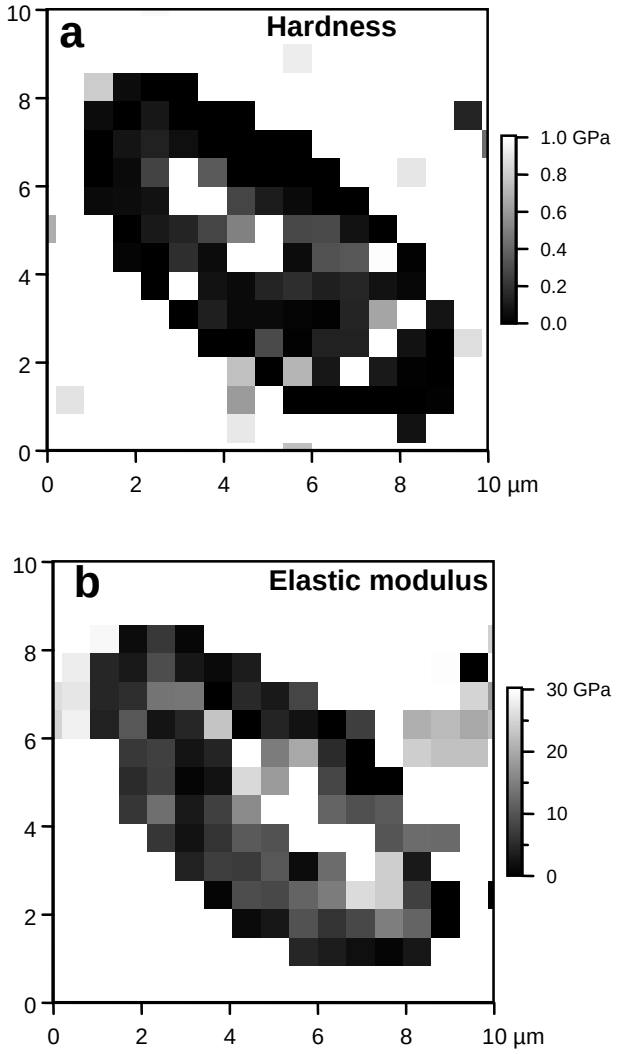

Fig. 9. Elasticity and hardness maps calculated from the force curves, as described in the text.

micromechanical properties of a selected diatom species. Special emphasis was paid to the AFM micromechanical measurement.

For plain AFM imaging of the frustules, both contact-mode and tapping-mode were used as imaging modes. Displaying the phase-angle changes in tapping-mode sometimes produces higher resolution images than the standard imaging. One simple explanation for the increased resolution, among several alternatives, is from geometric considerations. The tip–sample force interaction varies from spot to spot on the surface when the tip end radius is of the same magnitude as the local surface roughness. Phase imaging is also known to distinguish areas of different surface stiffness. However, quantitative interpretation of the stiffness from phase images is difficult. Other workers have tried to describe the response of the tapping tip (Burnham *et al.*, 1997) and the interpretation of phase data (Magonov *et al.*, 1997; Cleveland *et al.*, 1998; Garcia *et al.*, 1998). Depending on the applied tapping amplitude, the phase shift is dominated by different interactions such as the adhesion or the elasticity of the sample. Therefore, the observed phase-angle changes in Fig. 4 may reflect lateral differences in frustule material elasticity. Presumably, the frustule is stiffer at the CN region and at the frustule ends.

The micromechanical properties, elasticity and hardness, were measured under ambient conditions on dried samples. It is not clear to what extent these measurements apply to living diatoms under physiological conditions. Two methods were used to extract images of elastic modulus from the force–volume data. The methods revealed the same overall elastic pattern but there were differences in absolute elastic modulus, especially on the hardest part of the frustules. One explanation for such differences is the large deflection of the AFM cantilever. At large deflections, the photodetector responds partly nonlinearly, and this is observed as a slightly bent force curve. However, we eliminated some of this discrepancy by only interpolating to the part of the force curve with linear photodetector response. Therefore, a more likely explanation for the differences in elastic modulus observed on very hard surfaces is from the calibration of the AFM cantilever. The cantilever was calibrated on a reference surface, which was defined to be infinitely hard. However, when the stiffness of the sample approaches that of the reference surface, the calibration is not appropriate for accurate calculations of elastic modulus. Hence, above a certain value, the calculated modulus approaches that of an infinitely stiff surface, i.e. we can only conclude that the surface is as stiff or stiffer than crystalline silicon. Another concern is that the micro-mechanic calculation assumes the elastic response to be purely due to deformation of the shell material. This assumption is probably valid at the CN and CR, where the elastic modulus is high, but not on the TR, where the shell is elastically deformed during the experiment. The measured hardness,

Fig. 8. Nanoindentation experiments on substrates and on diatom frustules. Note the different scales on the images. The left column (a–d) shows parts of the raster-patterned indentations created on reference materials at different maximum loads (11–54 μN). The indents created with negligible tip-sliding (see text) are marked with an arrow. Note also that (b) shows indents made at two different loads (16 and 54 μN). The images to the right (e–h) show indents created on diatom frustules under the same conditions. Calculated hardness values are given in GPa and the locations are indicated with an arrow. A > indicates that the indent was created with non-negligible tip-sliding. The dashed arrow in (g) indicates a typical indent on the substrate mica surface at the same load.

on the other side, is independent of any shell deformation and is a parameter directly related to the material structure.

To interpret the results, one should bear in mind the current knowledge of silica shell wall growth (Chiappino & Volcani, 1977). The sequential development begins with the primary band and the differentiation of the CN. The initial location of the CN corresponds to the measured area of maximum elasticity and hardness. The location of our highest values coincides with frustule electron-dense areas measured at early development stages by SEM (Chiappino & Volcani, 1977). The microstructure of small hillocks on the CN may originate from initially larger knolls in which interstitial spaces have been filled during the development. These structures have higher contrast in phase imaging. However, the hillocks are very small and may also reflect the natural roughness of the coated silica.

The valves of diatoms are made of a matrix of amorphous silica gel. It is commonly believed that the frustule has unique molecular structures, which not are identical among species. Moreover, carbohydrates and proteins are present in, or at least associated with, the silica matrix (Vrieling *et al.*, 1999). Powder diffraction methods have revealed some of the bonds in overall *N. pelliculosa* frustule silica (Perry, 1989), although the form of the silica is unknown. Our results reveal frustule regions with possibly different structures of silica and degree of silicification. The occurrence of small domains of crystalline phases is only speculative (Pickett-Heaps *et al.*, 1990) and our measurements do not rule out such cryptocrystalline phases at the CN, which we measured to have a hardness approaching that of known crystalline phases.

Conclusion

We have studied the structure and micromechanical properties of diatom frustules. Unlike other experimental techniques, the AFM could be used to measure hardness and elasticity variations with a very high spatial resolution on small delicate structures such as diatom frustules. Moreover, the measurements are accompanied by simultaneous imaging of their delicate morphology.

The specific results for the model diatom *N. pelliculosa* reveal the overall geometry, the frustule microstructure and the local micromechanical properties. Basic structural information is revealed with a minimum of sample preparation. Hence, if the frustules are further cleaned from their organic coating, ultra-fine AFM structural studies could provide a simple method for detailed taxonomic classification. We have shown that AFM imaging allows visualization of the striae and their coalescence at the valve margins.

It was possible to measure micromechanical properties with the desired spatial resolution, but it required a careful selection of suitable AFM cantilevers. The different AFM instrumental configurations and evaluation methods gave the same results of semi-quantitative hardness and, at least partly, elasticity maps of the frustule. The lateral variations of the frustule micromechanical properties could be described. Moreover, the results correspond to characteristic features appearing in the different stages of the shell's growth. In general, the measured elastic modulus is higher along some part of the CR and at the CN, where it is higher at the curved-end side of the RF, the maximum values approaching that of pure silicon. The hardness, which is directly related to the material structure, is also higher on the CN and especially at the curved-end side of the RF. The hardness of the CR is fairly uniformly distributed, but with significantly lower values. It is clear that the CR and CN together act as a central load-bearing beam, of harder and stiffer material, along the length of the diatom.

We have shown that AFM can be used for complementary structural and micromechanical studies of diatom biomineralization. It is encouraging that the standard atomic force microscope, at least semi-quantitatively, can measure the micromechanical properties even on hard glass-like materials. We believe that the necessary steps to gain further understanding in biomineralization are: (i) to improve the instrumentation and use newly developed microscopes for micromechanical measurements. The most important improvements are hardware elimination of effects from drift and hysteresis of the z-piezo tube, but also from removal of the unwanted tip-sliding; (ii) to compare the properties of several species, also under physiological conditions; and (iii) to further study the organic coating.

Acknowledgements

This work was performed under the Swedish Research Council for Engineering Sciences (TFR) under contract 98-215; National Science Foundation, Materials Research Laboratory under award NSF-DMR-96-32716, NSF-DMR-96-22169, the Army Research office, MURI Program, DAAH04-96-1-0443. We thank Digital Instruments for support.

References

A-Hassan, E., Heinz, W.F., Antonik, M.D., D'Costa, N.P., Nageswaran, S., Schoenenberger, C.A. & Hoh, J.H. (1998) Relative microelastic mapping of living cells by atomic force microscopy. *Biophys. J.* **74**, 1564–1578.

Almqvist, N., Thomson, N.H., Smith, B.L., Stucky, G.D., Morse, D.E. & Hansma, P.K. (1999) Methods for fabricating and characterizing a new generation of biomimetic materials. *Mater. Sci. Eng.* **C7**, 37–43.

Bhushan, B. & Koinkar, V.N. (1994) Nanoindentation hardness

measurements using atomic force microscopy. *Appl. Phys. Lett.* **64**, 1653–1655.

Bhushan, B. & Koinkar, V.N. (1996) Microtribological studies of doped single-crystal silicon and polysilicon films for MEMS devices. *Ninth International Workshop on Micro Electromechanical Systems, San Diego, CA, USA*, pp. 91–102.

Bhushan, B., Kulkarni, A.V., Bonin, W. & Wyrobek, J.T. (1996) Nanoindentation and picoindentation measurements using a capacitive transducer system in atomic force microscopy. *Phil. Mag. A*, **74**, 1117–1128.

Burnham, N.A., Behrend, O.P., Oulevey, F., Gremaudi, G., Gallo, P.J., Gourdon, D., Dupas, E., Kulik, A.J., Pollock, H.M. & Briggs, G.A.D. (1997) How does a tip tap? *Nanotechnology*, **8**, 67–75.

Burnham, N.A. & Colton, R.J. (1989) Measuring the nanomechnical properties and surface forces of materials using an atomic force microscope. *J. Vac. Sci. Technol. A*, **7**, 2906–2913.

Busby, W.F. & Lewin, J.C. (1967) Silicate uptake and silica shell formation by synchronously dividing cells of the diatom *Navicula pelliculosa* (Breb.) Hilse. *J. Phycol.* **3**, 127–131.

Chiappino, M.L. & Volcani, B.E. (1977) Studies on the biochemistry and fine structure of silica shell formation in diatoms. VII. Sequential cell wall development in the pennate *Navicula pelliculosa*. *Protoplasma*, **93**, 205–221.

Cleveland, J.P., Anczykowski, B., Schmid, A.E. & Elings, V.B. (1998) Energy dissipation in tapping-mode atomic force microscopy. *Appl. Phys. Lett.* **72**, 2613–2615.

Drechsler, D., Karbach, A. & Fuchs, H. (1998) Nanoindentation on polycarbonate/polymethyl methacrylate blends. *Appl. Phys. A*, **66**, 825–829.

Garcia, R., Tamayo, M., Calleja, M. & Garcia, F. (1998) Phase contrast in tapping-mode scanning force microscopy. *Appl. Phys. A*, **66**, S309–S312.

Göken, M. & Kempf, M. (1998) Microstructural properties of superalloys investigated by nanoindentations in an atomic force microscope. *Acta Mater.* **47**, 1043–1052.

Gordon, R. & Drum, R.W. (1994) The chemical basis of morphogenesis. *Int. Rev. Cytol.* **150**, 243–372.

Gracias, D.H. & Somorjai, G.A. (1998) Continuum force microscopy study of the elastic modulus, hardness and friction of polyethylene and polypropylene surfaces. *Macromolecules*, **31**, 1269–1276.

Hoagland, K.D., Rosowski, J.R., Gretz, M.R. & Roemer, S.C. (1993) Diatom extracellular polymeric substances – function, fine-structure, chemistry, and physiology. *J. Phycol.* **29**, 537–566.

Ikai, A. (1996) STM and AFM of bio/organic molecules and structures. *Surf. Sci. Reports*, **26**, 205–259.

Kempf, M., Göken, M. & Vehoff, H. (1998) Nanohardness measurements for studying local mechanical properties of metals. *Appl. Phys. A*, **66**, S843–S846.

Laney, D.E., Garcia, R.A., Parsons, S.M. & Hansma, H.G. (1997) Changes in the elastic properties of cholinergic synaptic vesicles as measured by atomic force microscopy. *Biophys. J.* **72**, 806–813.

Linder, A., Colchero, J., Apell, H.J., Marti, O. & Mlynek, J. (1992) Scanning force microscopy of diatom shells. *Ultramicroscopy*, **42**, 329–332.

Magonov, S.N., Elings, V. & Whangbo, M.H. (1997) Phase imaging and stiffness in tapping-mode atomic force microscopy. *Surf. Sci.* **375**, L385–L391.

Morse, D.E. (1999) Silicon biotechnology: harnessing biological silica production to construct new materials. *Trends Biotechnol.* **17**, 230–232.

Nakajima, K., Yamaguchi, H., Jeong-Chang, L., Kageshima, M., Ikehara, T. & Nishi, T. (1996) Nanorheology of polymer blends investigated by atomic force microscopy. *4th International Colloquium on Scanning Tunneling Microscopy, Kanazawa, Japan*, pp. 3850–3854.

Nie, H.Y., Motomatsu, M., Mizutani, W. & Tokumoto, H. (1995) Local elasticity measurement on polymers using atomic force microscopy. *International Symposium on Ultra Materials for Picotransfer, Chiba, Japan*, pp. 143–148.

Perry, C.C. (1989) Chemical studies of biogenic silica. *Biomineralization: Chemical and Biochemical Perspectives* (ed. by S. Mann, J. Webb and R. J. P. Williams), pp. 223–256. VCH, New York.

Pickett-Heaps, J., ed. (1990) *Progress in Phycological Research*. Biopress Ltd, Bristol.

Pickett-Heaps, J., Schmid, A.M. & Edgar, L.A. (1990) The cell biology of diatom valve formation. *Progr. Phycol. Res.* **7**, 1–168.

Radmacher, M., Fritz, M., Cleveland, J.P., Walters, D.A. & Hansma, P.K. (1994) Imaging adhesion forces and elasticity of lysozyme adsorbed on mica with the atomic-force microscope. *Langmuir*, **10**, 3809–3814.

Radmacher, M., Fritz, M. & Hansma, P.K. (1995) Imaging soft samples with the atomic force microscope: gelatin in water and propanol. *Biophys. J.* **69**, 264–270.

Radmacher, M., Fritz, M., Kacher, C.M., Cleveland, J.P. & Hansma, P.K. (1996) Measuring the viscoelastic properties of human platelets with the atomic force microscope. *Biophys. J.* **70**, 556–567.

Randall, N.X., Christoph, R., Droz, S. & Julia-Schmutz, C. (1996) Localised micro-hardness measurements with a combined scanning force microscope/nanoindentation system. *Thin Solid Films*, **291**, 348–354.

Reimann, B.E.F., Lewin, J.C. & Volcani, B.E. (1966) Studies on the biochemistry and the fine structure of silica shell formation in diatoms. II. The structure of the cell wall of *Navicula pelliculosa* (Breb.) Hilse. *J. Phycol.* **2**, 74–84.

Robinson, D.H. & Sullivan, C.W. (1987) How do diatoms make biominerals? *Trends Biochem. Sci.* **12**, 151–154.

Round, F.E., Crawford, R.M. & Mann, D.G. (1990) *Diatoms*. Cambridge University Press, Cambridge.

Schaffer, T.E., Ionescu-Zanetti, C., Proksch, R., Fritz, M., Walters, D.A., Almqvist, N., Zaremba, C.M., Belcher, A.M., Smith, B.L., Stucky, G.D., Morse, D.E. & Hansma, P.K. (1997) Does abalone nacre form by heteroepitaxial nucleation or by growth through mineral bridges? *Chem. Mater.* **9**, 1731–1740.

Schoeman, F.R., Archibald, R.E.M. & Barlow, D.J. (1976) Structural observations and notes on the freshwater diatom *Navicula pelliculosa*. *Br. Phycol. J.* **11**, 251–263.

Smith, B.L., Schäffer, T.E., Viani, M., Thompson, J.B., Frederick, N.A., Kindt, J., Belcher, A., Stucky, G.D., Morse, D.E. & Hansma, P.K. (1999) Molecular mechanistic origin of the

toughness of natural adhesives, fibres and composites. *Nature*, **399**, 761–763.

Sneddon, I.N. (1965) The relation between load and penetration in the axisymmetric Boussinesq problem for a punch of arbitrary profile. *Int. J. Engng Sci.* **3**, 47–57.

Van de Poll, W.H., Vrieling, E.G. & Gieskes, W.W.C. (1999) Location and expression of frustulins in the pennate diatoms *Cylindrothea fusuformis*, *Navicula pelliculosa* and *Navicula salinarum*. *J. Phycol.* **35**, 1044–1053.

Vanlandingham, M.R., McKnight, S.H., Palmese, G.R., Eduljee, R.F., Gillespie, J.W. & McCulough, R.L. Jr (1997a) Relating elastic modulus to indentation response using atomic force microscopy. *J. Mater. Sci. Lett.* **16**, 117–119.

Vanlandingham, M.R., McKnight, S.H., Palmese, G.R., Elings, J.R., Huang, X., Bogetti, T.A., Eduljee, R.F. & Gillespie, J.W. (1997b) Nanoscale indentation of polymer systems using the atomic force microscope. *J. Adhesion*, **64**, 31–59.

Vrieling, E.G., Beelen, T.P.M., van Santen, R.A. & Gieskes, W.W.C. (1999) Diatom silicon biomineralization as an inspirational source of new approaches to silica production. *J. Biotechnol.* **70**, 39–51.

Werner, D., ed. (1977) *The Biology of Diatoms*. Blackwell, Oxford.

Weyn, B., Kalle, W., Kumar-Singh, S., VanMarck, E., Tanke, H. & Jacob, W. (1998) Atomic force microscopy: influence of air drying and fixation on the morphology and viscoelasticity of cultured cells. *J. Microsc.* **189**, 172–180.